Fourier-Transform Atomic Force Microscope-Based

Photothermal Infrared Spectroscopy with Broadband

Source

Qing Xie and Xiaoji G. Xu*

Department of Chemistry, Lehigh University, 6 E Packer Ave. Bethlehem, PA, 18015, United States

Keywords: AFM-IR, Fourier Transform, Nano-IR, Time-domain, Photothermal, Vibrational Spectroscopy, PFIR

Abstract: The mechanical detection of photothermal expansion from infrared (IR) absorption with an atomic force microscope (AFM) bypasses Abbe's diffraction limit, forming the chemical imaging technique of AFM-IR. Here, we develop a Fourier transform AFM-IR technique with peak force infrared (PFIR) microscopy and broadband femtosecond IR pulses. A Michelson interferometer creates a pair of IR pulses with controlled time delays to generate photothermal signals transduced by AFM to form an interferogram. A Fourier transform is performed to recover IR absorption spectra. We demonstrate the Fourier transform AFM-IR microscopy on polymer blend and hexagonal boron nitrides. An intriguing observation is the vertical asymmetry of the interferogram, which suggests the presence of multiphoton absorption processes under the tip-enhancement and femtosecond IR lasers. Our method demonstrates the feasibility of time-domain detection of AFM-IR signal in the mid-IR regime and paves the way towards multiphoton vibrational spectroscopy at the nanoscale below the diffraction limit.

Infrared (IR) microscopy spatially maps the distribution of chemical composition according to infrared resonances. Abbe's diffraction limit describes that the spatial resolution of traditional IR microscopy cannot exceed half of the light wavelength, on the order of micrometers. Spectra from tiny and clustered features cannot be spatially resolved. One increasingly popular way to bypass Abbe's diffraction limit is via integrating an atomic force microscope (AFM) with IR lasers. The sharp apex of the metal-coated AFM tip locally enhances the IR field to tens of nanometers scale that excites samples underneath, which is smaller than the free-space IR wavelength. The recent development of AFM-based nano-infrared (nano-IR) microscopies routinely deliver spatial resolutions of down to ten nanometers. Two main categories of nano-IR microscopy exist: the infrared scattering-type scanning near-field optical microscopy (s-SNOM) with optical detection; and the photothermal AFM-based infrared microscopy, commonly known as AFM-IR.

Different modes of nano-IR microscopy require different characteristics of light sources. For example, IR s-SNOM usually uses a high repetition rate or continuous source for its requirement of lock-in detection. A narrowband IR source is used for imaging; a broadband source is used for nano-FTIR spectroscopy that utilizes an asymmetric Michelson interferometer for signal detection.^{8, 9} Broadband IR radiations can come from many sources, from different frequency generations (DFG) of femtosecond laser pulses, synchrotron radiation, to blackbody radiations including plasma sources.¹⁰⁻¹⁴ In comparison, AFM-IR measures cantilever oscillations caused by photothermal expansion of the sample under IR pulses. A short-duration pulse serves as a trigger to generate photothermal expansions for detection. On the other hand, AFM-IR requires a narrowband laser source for both imaging and spectroscopy. A popular choice is a quantum cascade laser (QCL) or nanosecond-duration optical parametric oscillator (OPO). In contrast,

broadband IR pulses are usually not used for AFM-IR microscopy, as it does not directly deliver spectral resolution required for spectroscopy. The typical way to generate a spectrum from a broadband light source is through time-domain detection with an interferogram followed by Fourier transform. As broadband visible radiation from a super-continuum has been demonstrated to generate time-domain photothermal signals detectable by AFM in contact mode, 15 can we incorporate broadband IR radiation for AFM-IR microscopy for spectroscopic information?

In this article, we develop a Fourier transform AFM-IR spectroscopy through peak force infrared (PFIR) microscopy with a broadband IR source. PFIR microscopy is one of three AFM-IR modes.^{3, 16} PFIR offers a good spatial resolution of < 10 nm while preserving the surface integrity of the sample. Also, PFIR is compatible with kHz-level low laser repetition rates that are common in DFG IR sources. We name the resulting method Fourier transform peak force infrared (FT-PFIR) spectroscopy and demonstrate it on structured polymers and phonon polaritons of hexagonal boron nitride (*h*-BN).

The apparatus of the FT-PFIR microscope is described in Figure 1a. The setup consisted of a peak force tapping (PFT) enabled AFM (Multimode 8, Bruker), a broadband DFG IR source, a custom-built Michelson interferometer, and customized time synchronization and signal acquisition assembly. The AFM was operated in the PFT mode at 2 kHz, with a peak force amplitude of 100 nm. The waveform of the z piezostage oscillation was routed from the AFM controller (Nanoscope V, Bruker) to a lock-in amplifier (MFLi, Zurich Instruments) acting as a phase lock loop (PLL). A phase-locked transistor-transistor logic (TTL) waveform was generated by the lock-in amplifier and reconditioned by a function generator to trigger the Yb:KGW amplifier (Pharos, Light Conversion) at 2 kHz to emit femtosecond laser pulses centered at 1030

nm of ~190 fs duration. The emission from the laser amplifier was used to pump an optical parametric amplifier (Orpheus-HP with DFG, Light Conversion) to generate frequency-tunable mid-infrared laser radiation. The IR laser output was beam-expanded and guided into a Michelson interferometer to create a pair of replicas of IR pulses. A translation stage (DDS100, Thorlabs) was operated in constant velocity mode to adjust the optical path of one arm of the interferometer, creating a time delay τ between the pulse pair. Recombined IR pulses were guided into the tip-sample region of the AFM by a set of mirrors and a parabolic mirror (25.4 mm focal distance with N.A. ~0.2). The combined pulse energy was ~40 nJ. The photothermal responses of the sample were created by the tip enhancement of a metal-coated AFM tip. The rapid mechanical expansion due to the photothermal effect excited the AFM cantilever to oscillate and was measured through the acquisition of the vertical deflection signal of the AFM cantilever. Figure 1b shows an averaged cantilever vertical deflection waveform which illustrates the AFM tip detachment, in contact, and withdrawn stages. The laser emission was synchronized to the tip-sample contact through the adjustment of TTL trigger timing. The photothermal responses due to IR absorption rapidly pushed the AFM tip upward and excited the cantilever's oscillations. The cantilever deflection signal was reconditioned with a signal amplifier (SR560, Stanford Research Systems) and acquired by a data acquisition card (PXI-5122, National Instruments). A cantilever deflection curve that contains photothermal-induced oscillations is shown in Figure 1c. We created a custom-written program to acquire, process and store signals. A polynomial fitting on the curvature of the deflection signal background was obtained in real time and was subtracted from the deflection signal to obtain cantilever oscillations from the photothermal responses of the sample (Figure 1d). Then a fast Fourier transform (FFT) was carried out to convert the cantilever oscillation signal into the corresponding frequency domain

(Figure 1e) around the cantilever oscillation frequency. We integrated the frequency domain response within a window (demarcated by two red dashed lines in Figure 1e) to obtain a single value to describe the photothermal-induced oscillation amplitude, which was used as the PFIR signal. In our FT-PFIR measurement, the time delay τ between the pulse pair was scanned while recording the PFIR signal.

An interferogram was obtained by correlating the optical path difference of the Michelson interferometer arms and the photothermal PFIR signal from the sample (Figure 1f). The interferogram from our photothermal FT-PFIR signal was observed as symmetric in time because a symmetric Michelson interferometer was used. FFT of the interferogram reveals the spectrum of the photothermal response in the frequency domain, which we call the FT-PFIR spectrum (Figure 1g). The frequency coverage of the spectrum depends on the central frequency, the bandwidth of the laser source and the IR resonances of the sample. An example is shown in Supplementary Figure S1.

Results. The polymethyl methacrylate (PMMA) and polystyrene (PS) polymer blend was used as a standard sample to demonstrate FT-PFIR microscopy. The measurements were carried out with a Pt-coated AFM tip (HQ:NSC 14, MikroMasch). Figure 2a indicates the maximum height of the polymer blend is around 37 nm. Figure 2b shows the adhesion map. To distinguish the chemical compositions, the PFIR images under 1724 cm⁻¹ and 1600 cm⁻¹ corresponding to the carbonyl (C=O) vibrations of PMMA and the aromatic ring tension of PS, are plotted in Figure 2c and Figure 2d, respectively. Thus, the higher dot (including its edge) comprises PMMA, and the plain surface is PS. According to this, the blue and orange dots (Figure 2a) are the sampling positions for the FT-PFIR experiment. For the data acquisition, for example, the interferogram of carbonyl vibration of PMMA (Figure 2e) is collected first. Then, the interferogram, when the tip

is withdrawn from the sample, was scanned under the same frequency range as the background (Supplementary Figure S3). Subtracting the two spectra generated from the FFT of the interferogram, the FT-PFIR spectrum is obtained (Figure 2g). From left to right, the FT-PFIR spectra centered at 1492 cm⁻¹ (aromatic ring bending of PS, the interferogram of which is shown in Figure 2f), 1600 cm⁻¹ and 1724 cm⁻¹ are comparable to the FTIR spectra from the bulk of the PMMA (blue shadow) and PS (orange shadow). The full FTIR spectra are plotted in Supplementary Figure S2.

h-BN is a two-dimensional material composed of boron atoms and nitride atoms, structurally similar to graphene. h-BN is an insulator, chemically inert and has high thermal conductivity. 17-19 h-BN has a phonon mode around 1360 cm⁻¹ and supports hyperbolic phonon polaritons, ^{20, 21} which can be launched by the field enhancement underneath the metallic AFM tip. The polaritonic waves propagate and are reflected at the h-BN edge. Depending on the traversed distance, a resonator is formed between the tip and edge that can accommodate integer multiple of a series of polariton wavelengths. IR frequencies that excite these resonant polaritons will be efficiently absorbed by the tip-sample configuration, thus leading to increased heat generation as the photothermal signals, manifested as bright fringes as the tip is scanned over the sample. The corresponding IR frequencies to the polaritons that match the resonator between the tip and h-BN edge appear as absorption peaks in the spectrum. The data here are collected with a gold-coated AFM tip (TAP150, Bruker) under a longer interferogram range. In Figure 3a, the height of the larger piece (left) and the other belt-shape are around 60 nm and 10 nm, respectively. The PFIR images are obtained under 1380 cm⁻¹ (Figure 3b), 1397 cm⁻¹ (Figure 3c) and 1410 cm⁻¹ (Figure 3d). The measured IR fringe pattern becomes denser in higher frequencies. The three FT-PFIR spectra (Figure 3f) were collected at the positions of 300 nm (blue, whose interferogram is shown in Figure 3e), 510 nm (orange) and 780 nm (green) from the edge of the larger *h*-BN flake along the white arrow in Figure 3a. The spectrum varies from each position on the *h*-BN due to different resonator length discussed above.

Discussion. Our FT-PFIR instrument demonstrates the feasibility of using broadband IR sources in Fourier transform AFM-IR microscopy. The advantage is that all segments of IR spectrum are obtained in one measurement. In regular AFM-IR microscopy with a narrowband IR source (e.g., QCL), spectrum collection requires sweeping IR wavelengths. The sweeping speed is proportional to the tunable range of the light source. The wider the spectra, the longer the sweeping process. In contrast, the acquisition time of interferograms for Fourier transform AFM-IR is fixed and decoupled from the spectral range. If ultra-broadband IR pulses become available, for instance, from laser-induced plasma sources, 22 data-collection time shall remain the same, whereas regular AFM-IR with a narrowband source would require the measurement time be proportional to its bandwidth. This is the equivalent of FTIR's Fellgett's advantage for AFM-IR.²³ Similarly, the spectral resolution of the FT-PFIR is determined by the scan range of the interferogram, which practically has no upper limit. In terms of frequency coverage, although the bandwidth of our IR source is limited to ~ 150 cm⁻¹ due to pump laser bandwidth and phasematching conditions of nonlinear crystals, the central wavelength of our DFG is widely tunable from 600 cm⁻¹ to 5000 cm⁻¹. In contrast, the frequency coverage of the QCL is limited by the tunability of its individual chips. Full mid-IR spectrum coverage would require large numbers of QCL chips, and some frequency regions are currently still not commercially available.

In the classical model of FTIR interferogram generation from two identical pulses, the maximal field intensity of the interferogram at the zero-path delay should be twice the sum of two separate intensities. The contrast generation mechanism is described in the following

derivation. A pair of identical but time-delayed pulses are generated by the Michelson interferometer. The complex field of a broadband pulse is described in the frequency domain as $E(\omega) = \sqrt{S(\omega)} \cdot e^{i\varphi(\omega)}$, where ω is the frequency; $S(\omega)$ is its spectrum; $\varphi(\omega)$ is the spectral phase. A replica of the same pulse delayed by τ is thus $E'(\omega,\tau) = \sqrt{S(\omega)} \cdot e^{i\varphi(\omega)+i\omega\tau}$. The total complex field $E_{total}(\omega,\tau)$ of the pulse pair is the complex sum of $E(\omega)$ and $E'(\omega,\tau)$, described by Equation (1):

$$E_{total}(\omega, \tau) = \sqrt{S(\omega)}e^{i\phi(\omega)}(1 + e^{i\omega\tau}) \tag{1}$$

Its total intensity is thus $I_{total}(\omega,\tau) = E_{total}(\omega,\tau) \cdot E_{total}^*(\omega,\tau)$, which is $I_{total}(\omega,\tau) = 2S(\omega)(1+\cos(\omega\tau))$. Note that it is independent of the spectral phase $\varphi(\omega)$. At $\tau=0$, the total intensity is thus four times of the spectrum of each pulse $I_{total}(\omega,0) = 4S(\omega)$. At non-zero τ , the spectrum of the total pulse pair exhibits spectral modulations. The interferogram generated by the pulse pair is obtained by integrating intensity at all available frequencies. The optically detected interferogram $S(\tau)$ is expressed in Equation (2):

$$S(\tau) = \int_{-\infty}^{\infty} I_{total}(\omega, \tau) d\omega \tag{2}$$

It can be proven that $S(\omega)$ and $S(\tau)$ are linked by Fourier transform.²⁴

Photothermal AFM-IR signal is proportional to the energy dissipation after IR absorption by vibrational levels. In a simplified model, the vibrational resonances can be approximated by a collection of dampened harmonic oscillators. In the frequency domain, they are expressed as a collection of complex Lorentzian functions: $A(\omega) = \sum \frac{a_n}{\omega - \omega_n - i\Gamma_n}$, with n being the number of resonances, and ω_n , a_n and Γ_n are the resonant frequency, peak strength, and peak half width of

the nth resonances, respectively. The IR absorbed by the sample from the illumination of the pulse pair, which is the eventual energy dissipation, is thus proportional to the product between the IR intensity $I_{total}(\omega, \tau)$ and the imaginary part of the vibrational resonance $A(\omega)$. In AFM-IR, besides absorption from vibrational resonances, there is non-sample specific photothermal responses from the AFM cantilever or tip-cone contributed to photothermal signal, which are independent of the frequency represented by a constant B. Therefore, the total photothermal signal $L(\omega)$ in the frequency domain has the proportionality shown in Equation (3):

$$L(\omega, \tau) = I_{total}(\omega, \tau) \cdot (imag(A(\omega)) + B)$$
(3)

Based on above equations, suppose the photothermal heat generation is proportional to the IR intensity, the resulting interferogram from photothermal detection should be symmetric in both lateral and vertical directions. Figure 4a shows a numerically simulated interferogram from pure optical interference based on Equation (2), and Figure 4b displays a numerically simulated interferogram from the imaginary part of vibrational resonance represented by Lorentzian functions according to Equation (3). Both exhibits vertically symmetric shapes in the numerically simulated interferogram. As a reference, we recorded the photothermal response from the AFM cantilever alone when the tip was withdrawn and high IR laser power was used. The resulting interferogram from the pure laser background is vertically symmetric (Supplementary Figure S1).

However, we observed asymmetric vertical shapes from the photothermal-detected interferograms from samples with IR resonance. It cannot be straightforwardly reproduced by the model above. How do we understand such a deviation from vertically symmetric interferograms of conventional FTIR? Similar vertically asymmetric interferograms were commonly observed in

interferences that involve multiphoton processes.²⁵ If the signal generation involves two-photon absorption, then the interferogram will exhibit vertical asymmetry. For example, in the autocorrelation of laser pulses through second harmonic generation, the interferogram is strongly asymmetric.²⁶ If we assume the detected signals were generated by the absorption of two photons, i.e., the signal generation is proportional to the square of field intensity, then the resulting interferogram would be vertically symmetric. A plot of a numerically-simulated interferogram from a two-photon absorption process is displayed in Figure 4c.

The vertical asymmetry of the interferogram indicates multi-photon pathways exist in our AFM-IR experiment with femtosecond pulses. Photothermal detection means that the total energy of all net absorbed photons are detected, instead of photons with certain frequencies. All population relaxation pathways contribute to heat accumulation. The heat can come from relaxation from the first vibrational excited state or from higher excited states. Thus, under femtosecond IR excitation, when the pulse duration is shorter than the vibrational relaxation time, a "ladder climbing" of sequentially-populating vibrational excited states is possible (Figure 4d). Molecules are excited by a photon from the ground state to the first excited state, and then absorb the second photon to reach the second excited state, and further. The collective population of all excited states leads to heat generation. Additional multiphoton absorption processes lead to deviation from one-photon linear absorption and give rise to vertical asymmetry in a photothermal interferogram.

The anharmonicity of the electronic potential energy surface usually causes slightly red-shifted frequencies of the upper vibrational transitions. Such redshifts are often several to several tens of wavenumbers, which are within the bandwidth of our IR pulses. The needed frequencies for "ladder climbing" are available. In comparison, conventional frequency-domain AFM-IR uses a

narrowband IR source, e.g., QCL. Only one vibrational transition is promoted by one laser frequency, unless a specially designed frequency-domain pump/probe configuration is employed.²⁷ Moreover, the metallic AFM tip can enhance the optical field intensity by two orders of magnitude or more due to the lightning rod effect. The combination of femtosecond pulse duration, broad bandwidth, and high field intensity means that multiphoton processes become favorable. The total heat generated thus has a nonlinear field intensity dependence, as exhibited by the vertical asymmetry of the interferogram.

While the vertically asymmetric shape of a photothermal interferogram indicates the presence of multiphoton processes, further unraveling of the exact processes would require further development of the time-domain AFM-IR methods. For example, leveraging the advantage of short-duration coherent IR pulses to create a pulse sequence that is routinely used in modern time-domain 2D IR spectroscopy.²⁸ In our work, two pulses are introduced by the Michelson interferometer. If four time-controlled pulses were created and coupled to the tip-sample region of the PFIR microscope, one could expect the total photothermal signal be dependent on the timing of the IR pulses—through modulation of the coherence between and populations of accessible vibrational levels. Analyzing such photothermal signals would provide rich spectroscopic information and unravel the exact pathways of multiphoton processes that depend on the molecular structures and mode coupling, from a nanoscopic area much smaller than Abbe's diffraction limit.

In sum, we have developed the time-domain AFM-IR spectroscopy in the mid-IR frequency regime through the Fourier transform peak force infrared microscopy. It demonstrates the feasibility of using broadband IR pulses for spectrally resolved photothermal spectroscopy. Further development of the peak force tapping-based AFM-IR platform may open the possibility

for time-domain two-dimensional nano-IR microscopy that shall provide both rich spectroscopic

information and high spatial resolution.

Materials. The polymer blend film is prepared through spin-coating of the 10 µL toluene

solution of the polymethyl methacrylate (PMMA) and polystyrene (PS) on a silicon surface with

a spin coater (KW-4A MicroNano Tools). The concentration is 12 mg/mL (PMMA: PS = 3:2, by

weight ratio). The spin-coater settings are 600 revolutions per minute (rpm) for 6 s and 2800 rpm

for 60 s. The hexagonal boron nitride (h-BN) was purchased (BLK-hBN-HPA, 2D

Semiconductors). The h-BN sample was prepared by exfoliation method with scotch tape and

transferred to a silicon substrate.

AUTHOR INFORMATION

Corresponding Author

Xiaoji G. Xu; Department of Chemistry, Lehigh University, 6 E Packer Ave. Bethlehem, PA,

18015, United States; Email: xgx214@lehigh.edu

Author

Qing Xie; Department of Chemistry, Lehigh University, 6 E Packer Ave. Bethlehem, PA, 18015,

United States

Author Contributions

X.G.X designed the concept of the FT-PFIR instrument. The experimental setup was built by

X.G.X. and Q.X. Q.X. did the experiment and perform data collection. The manuscript was

written together by X.G.X. and Q.X. X.G.X. oversaw the research.

ACKNOWLEDGMENTS

12

We would like to thank Dr. Yin Song for consultation on suitable translation stages for interferogram collections, and Dr. Martin Zanni for discussions on time domain photothermal detections and implications on possibility on 2D spectroscopy. We would like to thank Dr. Haomin Wang, Andrea Dorsa, and Amirhossein Zahmatkeshsaredorahi for proofreading the manuscript. X. G. X. would like to thank the support from Beckman Young Investigator Award from the Arnold and Mabel Beckman Foundation, the Sloan Research Fellowship from the Alfred P. Sloan Foundation, and the Camille Dreyfus Teacher-Scholar Award from the Camille and Henry Dreyfus Foundation. Q.X. and X. G. X. would also like to thank the support from the National Science Foundation, award number CHE 1847765.

REFERENCES

- (1) Abbe, E., Beiträge zur Theorie des Mikroskops und der mikroskopischen Wahrnehmung. Archiv für mikroskopische Anatomie 1873, 9 (1), 413-468.
- (2) Keilmann, F.; Hillenbrand, R., Near-field microscopy by elastic light scattering from a tip. Philosophical Transactions of the Royal Society of London. Series A: Mathematical, Physical and Engineering Sciences 2004, 362 (1817), 787-805.
- (3) Mathurin, J.; Deniset-Besseau, A.; Bazin, D.; Dartois, E.; Wagner, M.; Dazzi, A., Photothermal AFM-IR spectroscopy and imaging: Status, challenges, and trends. Journal of Applied Physics 2022, 131 (1), 010901.
- (4) Wang, L.; Wang, H.; Wagner, M.; Yan, Y.; Jakob, D. S.; Xu, X. G., Nanoscale simultaneous chemical and mechanical imaging via peak force infrared microscopy. Science Advances 2017, 3 (6), e1700255.

- (5) Nowak, D.; Morrison, W.; Wickramasinghe, H. K.; Jahng, J.; Potma, E.; Wan, L.; Ruiz, R.; Albrecht Thomas, R.; Schmidt, K.; Frommer, J.; Sanders Daniel, P.; Park, S., Nanoscale chemical imaging by photoinduced force microscopy. Science Advances 2 (3), e1501571.
- (6) Mathurin, J.; Pancani, E.; Deniset-Besseau, A.; Kjoller, K.; Prater, C. B.; Gref, R.; Dazzi, A., How to unravel the chemical structure and component localization of individual drugloaded polymeric nanoparticles by using tapping AFM-IR. Analyst 2018, 143 (24), 5940-5949.
- (7) Chen, X.; Hu, D.; Mescall, R.; You, G.; Basov, D. N.; Dai, Q.; Liu, M., Modern scattering-type scanning near-field optical microscopy for advanced material research. Advanced Materials 2019, 31 (24), 1804774.
- (8) Huth, F.; Govyadinov, A.; Amarie, S.; Nuansing, W.; Keilmann, F.; Hillenbrand, R., Nano-FTIR absorption spectroscopy of molecular fingerprints at 20 nm spatial resolution. Nano Letters 2012, 12 (8), 3973-3978.
- (9) Amarie, S.; Keilmann, F., Broadband-infrared assessment of phonon resonance in scattering-type near-field microscopy. Physical Review B 2011, 83 (4), 045404.
- (10) Hermann, P.; Hoehl, A.; Patoka, P.; Huth, F.; Rühl, E.; Ulm, G., Near-field imaging and nano-Fourier-transform infrared spectroscopy using broadband synchrotron radiation. Optics express 2013, 21 (3), 2913-2919.
- (11) Bechtel, H. A.; Muller, E. A.; Olmon, R. L.; Martin, M. C.; Raschke, M. B., Ultrabroadband infrared nanospectroscopic imaging. Proceedings of the National Academy of Sciences 2014, 111 (20), 7191-7196.

- (12) Wagner, M.; Jakob, D. S.; Horne, S.; Mittel, H.; Osechinskiy, S.; Phillips, C.; Walker, G. C.; Su, C.; Xu, X. G., Ultrabroadband nanospectroscopy with a laser-driven plasma source. ACS Photonics 2018, 5 (4), 1467-1475.
- (13) Lahneman, D. J.; Huffman, T. J.; Xu, P.; Wang, S. L.; Grogan, T.; Qazilbash, M. M., Broadband near-field infrared spectroscopy with a high temperature plasma light source. Optics Express 2017, 25 (17), 20421-20430.
- (14) Huth, F.; Schnell, M.; Wittborn, J.; Ocelic, N.; Hillenbrand, R., Infrared-spectroscopic nanoimaging with a thermal source. Nature Materials 2011, 10 (5), 352-356.
- (15) Bohlmann Kunz, M.; Podorova, Y.; Armstrong, Z. T.; Zanni, M. T., Time-Domain Photothermal AFM Spectroscopy via Femtosecond Pulse Shaping. Analytical Chemistry 2022, 94 (36), 12374-12382.
- (16) Wang, L.; Wang, H.; Xu, X. G., Principle and applications of peak force infrared microscopy. Chemical Society Reviews 2022, 51 (13), 5268-5286.
- (17) Zhang, K.; Feng, Y.; Wang, F.; Yang, Z.; Wang, J., Two dimensional hexagonal boron nitride (2D-hBN): synthesis, properties and applications. Journal of Materials Chemistry C 2017, 5 (46), 11992-12022.
- (18) Liu, Z.; Gong, Y.; Zhou, W.; Ma, L.; Yu, J.; Idrobo, J. C.; Jung, J.; MacDonald, A. H.; Vajtai, R.; Lou, J., Ultrathin high-temperature oxidation-resistant coatings of hexagonal boron nitride. Nature Communications 2013, 4 (1), 1-8.

- (19) Caldwell, J. D.; Aharonovich, I.; Cassabois, G.; Edgar, J. H.; Gil, B.; Basov, D., Photonics with hexagonal boron nitride. Nature Reviews Materials 2019, 4 (8), 552-567.
- (20) Geick, R.; Perry, C.; Rupprecht, G., Normal modes in hexagonal boron nitride. Physical Review 1966, 146 (2), 543.
- (21) Dai, S.; Fei, Z.; Ma, Q.; Rodin, A.; Wagner, M.; McLeod, A.; Liu, M.; Gannett, W.; Regan, W.; Watanabe, K., Tunable phonon polaritons in atomically thin van der Waals crystals of boron nitride. Science 2014, 343 (6175), 1125-1129.
- (22) Huang, J.; Parobek, A.; Ganim, Z., Octave-spanning mid-infrared pulses by plasma generation in air pumped with an Yb: KGW source. Optics Letters 2016, 41 (21), 4855-4858.
- (23) Fellgett, P. B., On the Ultimate Sensitivity and Practical Performance of Radiation Detectors. Journal of the Optical Society of America, 1949, 39 (11), 970-976.
- (24) Cohen, J., Introduction to Fourier Transform Spectroscopy. US Department of Commerce, National Bureau of Standards: 1986.
- (25) Müller, M.; Squier, J.; Brakenhoff, G., Measurement of femtosecond pulses in the focal point of a high-numerical-aperture lens by two-photon absorption. Optics Letters 1995, 20 (9), 1038-1040.
- (26) Roth, J. M.; Murphy, T. E.; Xu, C., Ultrasensitive and high-dynamic-range two-photon absorption in a GaAs photomultiplier tube. Optics Letters 2002, 27 (23), 2076-2078.
- (27) Wang, H.; Xie, Q.; Zhang, Y.; Xu, X. G., Photothermally Probing Vibrational Excited-State Absorption with Nanoscale Spatial Resolution through Frequency-Domain Pump-Probe

Peak Force Infrared Microscopy. The Journal of Physical Chemistry C 2021, 125 (15), 8333-8338.

(28) Hamm, P.; Zanni, M., Concepts and methods of 2D infrared spectroscopy. Cambridge University Press: 2011.

FIGURES

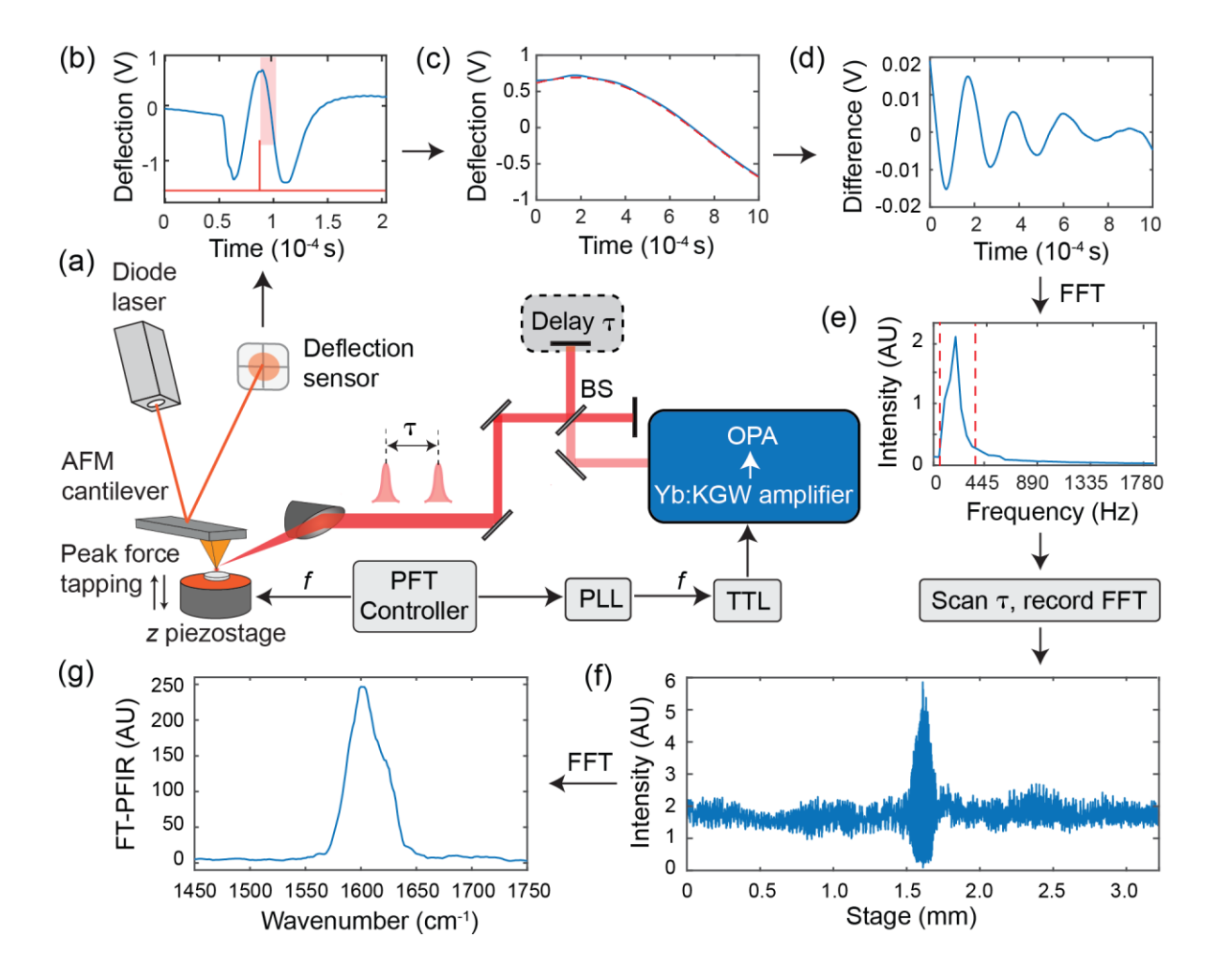


Figure 1. (a) Instrument setup of the Fourier-transform Peak Force Infrared (FT-PFIR) microscope. OPA: optical parametric amplifier. (b) Cantilever deflection curve (blue) of one PFT cycle and its corresponding laser illumination (red) under the same trigger frequency (2 kHz). (c) is the zoomed-in section of the cantilever deflection curve in (b) when the tip is in contact with the sample surface. The red dashed line shows the 4th-order polynomial fit of the deflection curve as a background envelope. (d) The photothermal-induced cantilever oscillation signal is the difference is obtained from subtracting the deflection curve and its envelope fitting. (e) PFIR signal from sample expansion underneath the tip calculated from the Fourier transform of (d). (f) is the interferogram by scanning the stage position at constant velocity and the corresponding PFIR signal. (g) FT-PFIR spectrum generated from the Fourier transform of the interferogram.

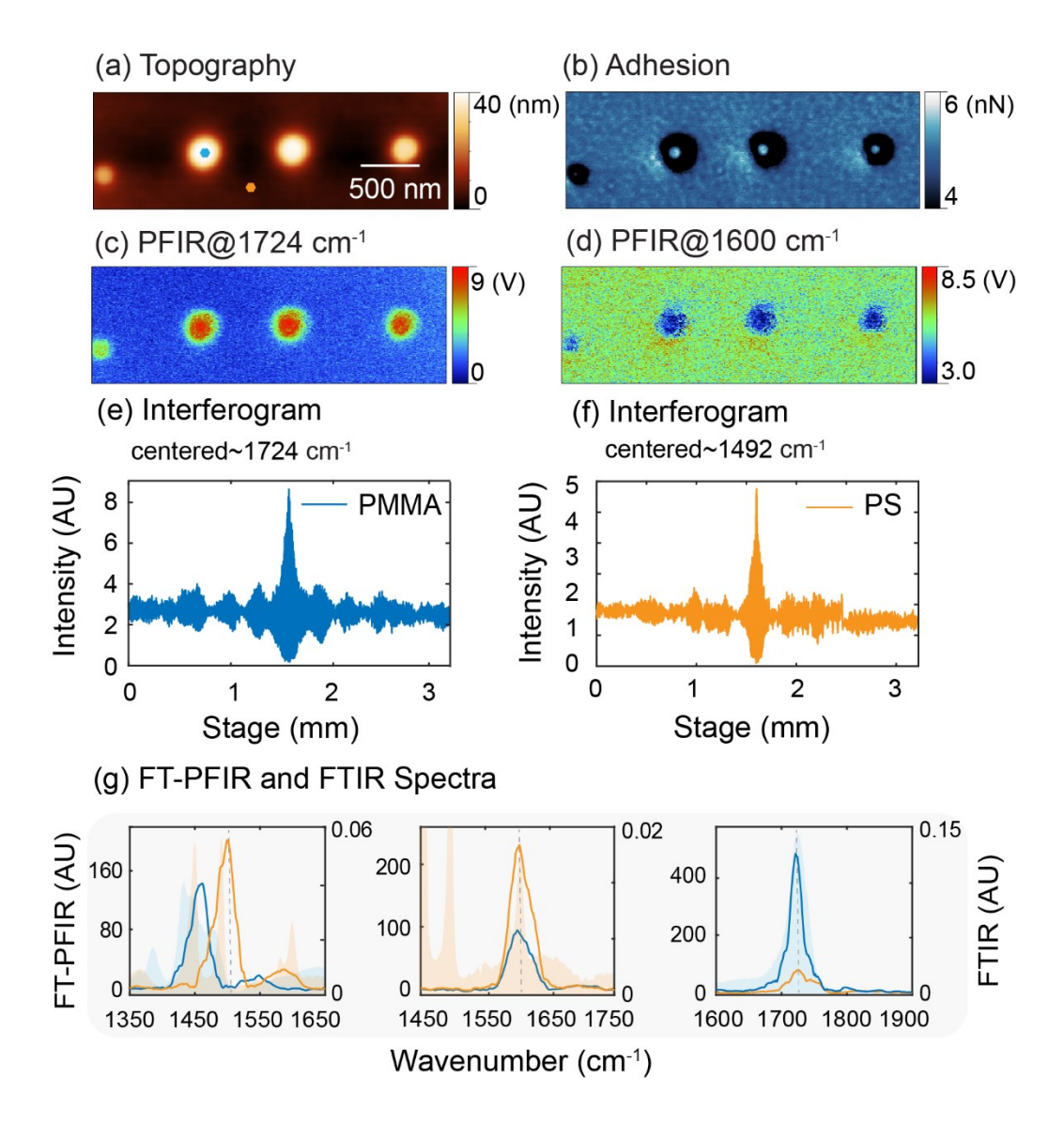


Figure 2. (a) Topography of polymer blend sample. The scale bar is 500 nm. (b) Adhesion image. (c) and (d) are the PFIR maps of the PMMA and PS under 1724 cm⁻¹ and 1600 cm⁻¹, respectively. (e) and (f) are the interferograms collected from the PMMA and PS marked with blue and orange in (a). (g) FT-PFIR of PMMA (blue) and PS (orange) collected under different frequency ranges. The FTIR spectra of PMMA and PS are included as blue and orange shades, respectively. The dashed line indicates the approximated center of the IR pulse bandwidth. The background has been subtracted. The spectra have been smoothed.

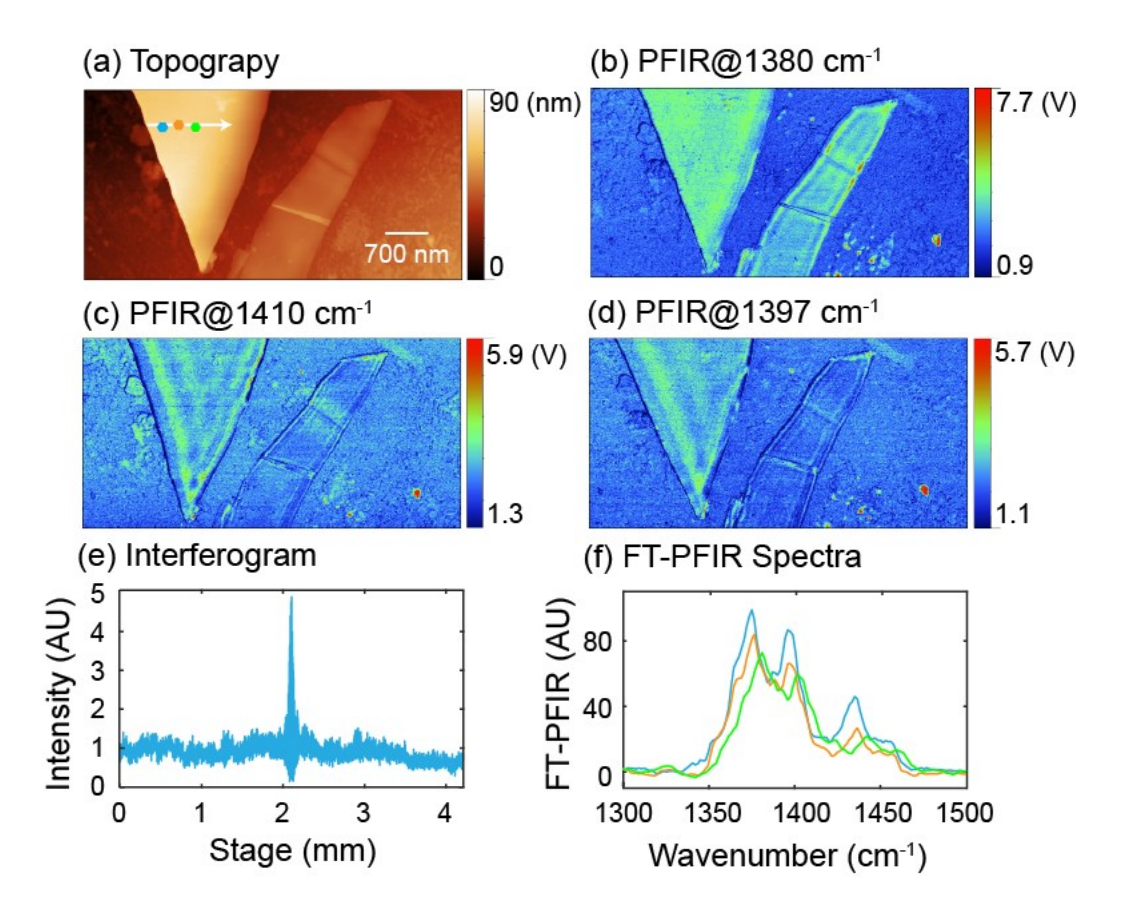


Figure 3. (a) Topography of h-BN sample on Si substrate. The scale bar is 700 nm. (b), (c) and (d) are the PFIR images of the sample under 1380 cm⁻¹, 1397 cm⁻¹ and 1410 cm⁻¹, respectively. (e) Interferogram at the position marked blue in (a). (f) FT-PFIR spectra collected along the white arrow in (a), the blue, orange and green show the positions at 300 nm, 510 nm and 780 nm from the edge of the h-BN, respectively. The background has been subtracted and the spectra have been smoothed. The corresponding interferograms can be find in Supplementary **Figure S4**.

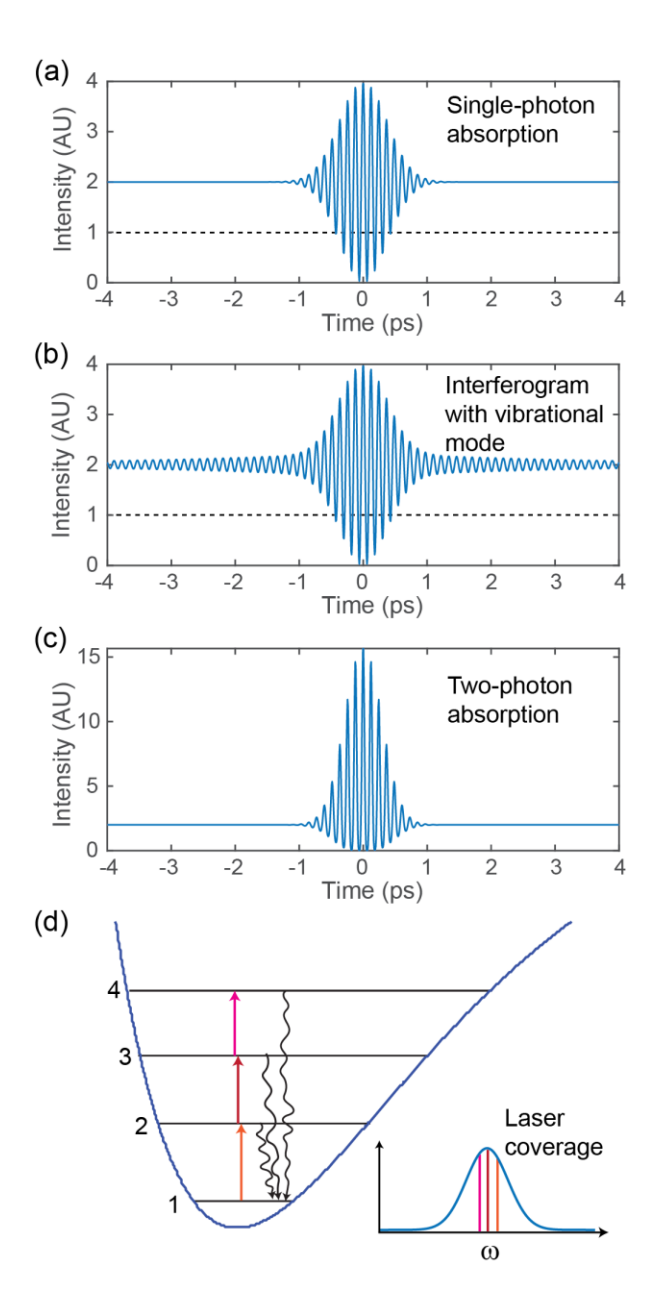


Figure 4. (a) Numerically simulated interferogram from pure optical interference. (b) Numerically simulated interferogram with a vibrational resonance. The interferograms in both (a) and (b) exhibit vertical symmetry. (c) Numerically simulated interferogram from a two-photon absorption process that exhibits strong vertical asymmetry. (d) Schematic of vibrational energy levels that illustrates the possibility of multiple-photon absorption under strong IR illumination.

ToC graphic

